OEA | Opto-Electronic Advances

Article

July 2026, Vol. 9, No. 7

Open Access

Parallel bright-field and multi-order edge imaging via wide field-of-view trichannel metalens

Xiaotong Li[1†], Yeseul Kim[1†], Youngsun Jeon[1†], Junhwa Seong[1], Jaekyung Kim[1], Peng Tang[1], Shiqi Hu[1], Harit Keawmuang[1], Beomha Yang[2], Dongmin Jeon[1], Le Dai[3], Weiyan Li[4,5], Xiaodong Cai[6], Jinhui Shi[4,5], Yong-Sang Ryu[7], Trevon Badloe[8,9]* and Junsuk Rho[1,2,3,10,11,12]*

Abstract: Modern optical systems require the capability to perform multi-functional and parallel imaging within compact, integrated architectures. However, conventional refractive lenses are bulky, restricted to single-mode operation, and incompatible with planar integration. In this work, we propose a trichannel metalens capable of simultaneously performing bright-field imaging, first-order edge detection, and second-order edge detection over a wide field-of-view (FOV). Specifically, by encoding combinations of input-output circular polarization, different functions are independently realized in three channels, and the spin-dependent gradient phase is employed to spatially separate them, ensuring that all three functions can be simultaneously captured under linearly polarized illumination, without necessitating mode switching or additional optical components. Experimental results show that the proposed metalens can parallelly provide three independent imaging functions with clear spatial separation and stable performance over a FOV ranging from −10° to 10°. Our approach offers a promising path toward compact, integrated imaging systems for biomedical imaging, real-time edge analysis, and machine vision applications.

Keywords: trichannel metalens; multi-functional imaging; wide field-of-view; edge detection; bioimaging

DOI: 10.29026/oea.2026.250306 | CSTR: 32247.14.oea.2026.250306

Citation: Li XT, Kim Y, Jeon Y et al. Parallel bright-field and multi-order edge imaging via wide field-of-view trichannel metalens. *Opto-Electron Adv* **9**, 250306 (2026).

1 Introduction

Focusing and imaging are essential operations in optical systems, significantly impacting science, engineering, and technology[1,2]. Generally, these functions are realized using refractive lenses, where the curvature and thickness of glass elements are delicately designed to manipulate light propagation and achieve the desired focal properties. However, these traditional lenses suffer from inherent limitations, such as large physical dimensions and complex assembly requirements, resulting in difficulties integrating with modern miniaturized and planar optical systems. Furthermore, their functionality is typically restricted to singular optical tasks, such as beam shaping, bright-field imaging or

Received: 8 November 2025

Accepted: 9 March 2026

Published online: 20 April 2026

[1]Department of Mechanical Engineering, Pohang University of Science and Technology (POSTECH), Pohang 37673, Republic of Korea; [2]Quantum Information Science Program, Graduate School of Convergence Science and Technology, Pohang University of Science and Technology (POSTECH), Pohang 37673, Republic of Korea; [3]Department of Electrical Engineering, Pohang University of Science and Technology (POSTECH), Pohang 37673, Republic of Korea; [4]Key Laboratory of In-Fiber Integrated Optics of Ministry of Education, College of Physics and Optoelectronic Engineering, Harbin Engineering University, Harbin 150001, China; [5]Key Laboratory of Photonic Materials and Devices Physics for Oceanic Applications, College of Physics and Optoelectronic Engineering, Harbin Engineering University, Harbin 150001, China; [6]Thin Film Optics R&D Center, Department of High-power Laser Optics Technology and Engineering, Shanghai Institute of Optics and Fine Mechanics, Chinese Academy of Sciences, Shanghai 201800, China; [7]School of Biomedical Engineering, Korea University, Seoul 02841, Republic of Korea; [8]Department of Electronics and Information Engineering, Korea University, Sejong 30019, Republic of Korea; [9]Digital Healthcare Center, Sejong Institute for Business and Technology, Korea University, Sejong 30019, Republic of Korea; [10]Department of Chemical Engineering, Pohang University of Science and Technology (POSTECH), Pohang 37673, Republic of Korea; [11]POSCO-POSTECH-RIST Convergence Research Center for Flat Optics and Metaphotonics, Pohang 37673, Republic of Korea; [12]National Institute of Nanomaterials Technology (NINT), Pohang 37673, Republic of Korea.

[†]These authors contributed equally to this work.

*Correspondence: T Badloe, E-mail: trevon@korea.ac.kr; J Rho, E-mail: jsrho@postech.ac.kr

edge detection, lacking the capability for multi-functional imaging and parallel optical image operations. These constraints pose significant challenges to the development of compact, multi-functional, and integrable optical systems.

Recently, the development of metasurfaces, planar optical elements composed of subwavelength microstructures (i.e., meta-atoms) arranged in specific sequences, has revolutionized the imaging domain and provided new opportunities to realize ultracompact meta-devices for multi-functional and parallel optical operations[3–13]. Utilizing propagation (PG), Pancharatnam-Berry (PB), resonant, or hybrid phase modulation mechanisms, scientists have demonstrated many fascinating phenomena, such as anomalous light deflection[14–18], the photonic spin-Hall effect[19–25], focusing[26–34], and holograms[35–40]. Moreover, by integrating active or phase-change materials into passive metasurfaces, one can obtain tunable meta-devices whose electromagnetic responses can be adjusted through external control signals[41–49]. Despite these advances, most still suffer from a narrow field-of-view (FOV), single-channel functionality, or reliance on external stimuli for image mode switching, making it difficult to meet the demand for multi-functional and parallel imaging with a wide-FOV on a static and compact platform, which is more useful in practical applications.

In this work, we propose a trichannel metalens for parallel bright-field imaging, first-order edge detection, and second-order edge detection over a wide-FOV. These three optical analog image processing functionalities are assigned to distinct channels through specific combinations of input-output circular polarization states. Specifically, Channel 1 (right-handed circular polarization input to left-handed circular polarization output, RCP-LCP) enables bright-field imaging, Channel 2 (RCP-RCP and LCP-LCP) performs first-order edge detection, and Channel 3 (LCP-RCP) achieves second-order edge detection. Moreover, by introducing a spin-dependent gradient phase, these three-channel images can be spatially separated and simultaneously captured within a single charge-coupled device (CCD) imaging area under linearly polarized (LP) illumination and detection. This configuration enables real-time and parallel multi-functional imaging without the need for dynamic switching mechanisms or additional optical components. Experimental results demonstrate that the metalens distinctly resolves the three imaging regions with high spatial separation and stable performance across a wide-FOV from -10° to 10°. The proposed metalens exhibits a numerical aperture (NA) of 0.503 and a focal length of 430 μm at a wavelength of 635 nm. The measured efficiencies are 41.7% for RCP-LCP in Channel 1, 25.1% for RCP-RCP and 28.3% for LCP-LCP in Channel 2, and 14.5% for LCP-RCP in Channel 3, respectively. These results highlight the potential of our approach for high-throughput image processing, real-time edge enhancement, and compact multi-modal optical systems.

2 Results

2.1 Principle

The schematic illustration of the proposed wide-FOV trichannel metalens for parallel bright-field and multi-order differential operation is shown in Fig. 1. This metalens modulates the incident object light field and generates three spatially separated imaging outputs at the same focal plane, enabling parallel bright-field imaging (Channel 1), first-order edge-enhanced imaging (Channel 2), and second-order edge-enhanced imaging (Channel 3), as illustrated in Fig. 1(a). The imaging functionality of each channel is associated with a distinct focusing-vortex response encoded in the transmitted wavefront, where the topological charges are 0, 1, and 2 for Channels 1–3, respectively. Figure 1(b) highlights the wide-FOV behavior of the trichannel metalens. Under LP illumination, the metalens forms three focused spots with different vortex orders in a common focal plane. When the incidence becomes oblique, these focal responses undergo a synchronized lateral translation while remaining separable, providing a deterministic angle-to-position mapping for wide-FOV operation. Furthermore, under circularly polarized illumination, the specific channels can be activated depending on the handedness of the input polarization. For instance, under RCP input, only Channels 1 and 2 are enabled, while Channel 3 remains suppressed due to it working under LCP-RCP condition. Conversely, under LCP input, Channels 2 and 3 are activated while Channel 1 is inactive. Similarly, in addition to controlling the input polarization, further channel selectivity can be achieved by detecting specific polarization states at the output, thereby enabling flexible choosing of imaging functionalities. This dual control strategy provides a powerful means to multiplex and demultiplex imaging channels within a single planar device.

The detailed design principle and phase profile corresponding to each channel are depicted in Fig. 1(c). By combining the PG and PB phases and properly utilizing the polarization-converted and polarization-preserved parts of output, the functionalities of different channels are flexibly modulated. Specifically, the spin-independent PG phase is utilized to realize the first-order edge detection of Channel 2 (corresponding to the part of the output where polarization is preserved), while also partially contributing to the phase modulation of Channels 1 and 3, which can be expressed as:

$$\Phi_{\mathrm{PG}}(r,\theta) = -k_0\left(\sqrt{r^2+F^2}-F\right)+\theta\,, \tag{1}$$

where (r,θ) are the polar coordinates at the metalens plane, $k_0 = 2\pi/\lambda$ is the vacuum wave vector, λ is the working wavelength, and F represents the focal length. In contrast, the PB phase introduces spin-dependent orbital angular momentum (OAM) and linear gradient phase for the polarization-converted part, which are responsible for decoupling the functionalities of these three channels and spatially

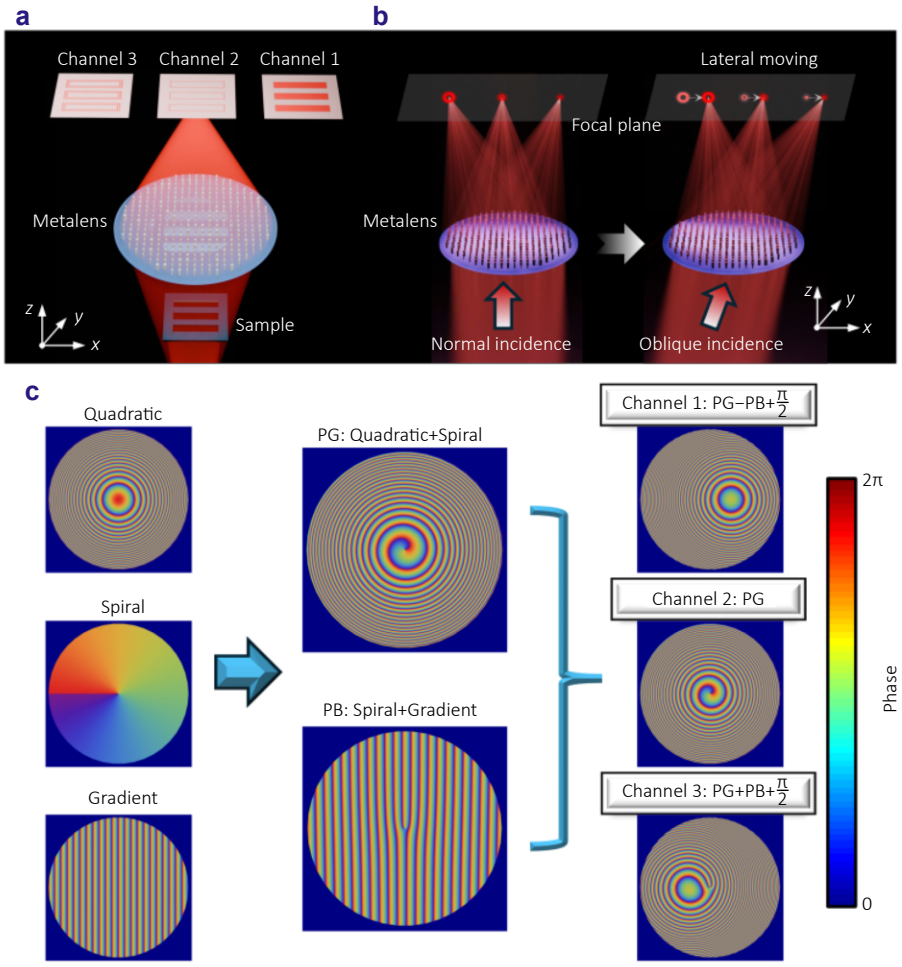


Fig. 1 | Operating principle and phase distribution of the wide-FOV trichannel metalens. (a) Schematic of parallel multi-modal imaging enabled by the proposed metalens. The meta-device modulates the incident object light field and generates three spatially separated imaging channels at the same focal plane, corresponding to bright-field imaging (Channel 1), first-order edge-enhanced imaging (Channel 2), and second-order edge-enhanced imaging (Channel 3). (b) Concept of wide-FOV operation. Under LP illumination, three focused responses with different vortex orders (topological charges l = 0, 1 and 2 for Channels 1–3, respectively) are formed in a common focal plane. Under oblique incidence, the three focal patterns move laterally while remaining distinguishable. (c) Phase design principle and distribution of the metalens. The phase is synthesized by combining a spin-independent PG component (quadratic focusing phase and spiral phase) and a spin-dependent PB component (spiral phase and linear gradient phase). The resulting phase profiles assigned to Channels 1–3 are shown on the right (the constant phase offset π/2 does not affect the imaging functionality).

separating them on the imaging plane that can be expressed as:

$$\Phi_{\mathrm{PB}}(r,\theta) = -k_0 r\cos\theta\sin\alpha + \theta\,, \tag{2}$$

where α represents the deflected angle of the linear gradient phase, which ensures that the three distinct images can be simultaneously and independently read out. In addition to spatial separation, the spiral phase embedded in the focusing wavefront plays a key role in enabling edge-enhanced imaging. For a metasurface imparting a vortex phase with topological charge l, the corresponding point spread function (PSF) exhibits an azimuthal phase singularity and a donut-shaped intensity profile. When such a PSF is convolved with the object field, destructive interference occurs in regions with uniform amplitude or phase, leading to suppressed intensity in homogeneous areas. In contrast, regions containing spatial variations, such as amplitude or phase gradients at object boundaries, break this symmetry and give rise to a strong intensity response. As a result, a focusing vortex with $l = 1$ effectively performs a first-order spatial differentiation, highlighting object edges. Similarly, a higher-order vortex ($l = 2$) produces a PSF that is more sensitive to higher-order spatial variations, enabling second-order edge enhancement with increased sensitivity to finer structural features. A rigorous theoretical derivation of the PSFs for different vortex orders and their corresponding edge detection mechanisms is provided in Supplementary Section 1.

Assuming that the meta-atom has high transmittance, based on the Jones matrix derivation, the final target phase

modulation of the metalens for different combinations of input-output circular polarization states can be obtained as:

$$\mathbf{J}=\begin{bmatrix} e^{i\Phi_{LCP-LCP}} & e^{i\Phi_{RCP-LCP}} \\ e^{i\Phi_{LCP-RCP}} & e^{i\Phi_{RCP-RCP}} \end{bmatrix}=\frac{1}{2}\begin{bmatrix} e^{i\Phi_{PG}(r,\theta)} & e^{i\left(\Phi_{PG}(r,\theta)-\Phi_{PB}(r,\theta)+\frac{\pi}{2}\right)} \\ e^{i\left(\Phi_{PG}(r,\theta)+\Phi_{PB}(r,\theta)+\frac{\pi}{2}\right)} & e^{i\Phi_{PG}(r,\theta)} \end{bmatrix}. \tag{3}$$

Notably, this constant phase difference $\pi/2$ does not influence the functional performance of the metalens in our design[30]. The detailed derivation of the Jones matrix is given in the Supplementary Seciton 2. Furthermore, to ensure a balanced intensity distribution between these three channels, the amplitude contributions from both the polarization-converted and polarization-preserved components should be equal. Based on these analyses, our meta-atom design follows two key criteria: 1) the transmission efficiencies for both polarization-converted and polarization-preserved components under circular polarization illumination should be close to 50%. 2) The phase modulation associated with the polarization-converted and polarization-preserved components should provide 0–2π phase coverage.

2.2 Meta-atom design

To identify optimal anisotropic meta-atom geometries that satisfy design requirements of the proposed trichannel metalens, a comprehensive parameter sweep is carried out using finite-difference time-domain (FDTD) simulations. The working wavelength was set to λ = 635 nm and low-loss hydrogenated amorphous silicon (a-Si:H) nanopillars on a silicon dioxide (SiO_2) substrate are employed to ensure the high optical transparency of the sample[50]. The measured refractive index of a-Si:H is shown in Supplementary Section 3. Figure 2(a) illustrates the schematic diagram of the meta-atom, which functions as a birefringent unit whose transmission properties, including both amplitude and phase, are highly sensitive to its geometric parameters. The square lattice period (p) is set to 350 nm to suppress high-order diffraction and satisfy the Nyquist-Shannon sampling theorem. Meanwhile, the height (h) of the nanopillar is fixed at 800 nm, while the length (l_x) and width (l_y) are swept from 80 to 250 nm to obtain sufficient phase coverage and suitable transmission performance, as shown in Fig. 2(b).

Based on the parameter sweep, a set of meta-atoms is selected to implement the proposed trichannel functionality. Their optical responses are shown in Fig. 2(c) using three-dimensional scatter plots, where each data point corresponds to one specific meta-atom geometry. The meta-atom index is used as an identifier to correlate the phase and transmission responses of the same structure in the polarization-preserved and polarization-converted channels (see Supplementary Section 4). As shown in Fig. 2(c), the selected meta-atoms collectively span the full 0–2π phase range while maintaining transmission efficiencies between approximately 0.2 and 0.6 in both polarization channels. This balanced amplitude response is a key requirement for stable and reliable trichannel operation, ensuring comparable energy levels among the different imaging functionalities.

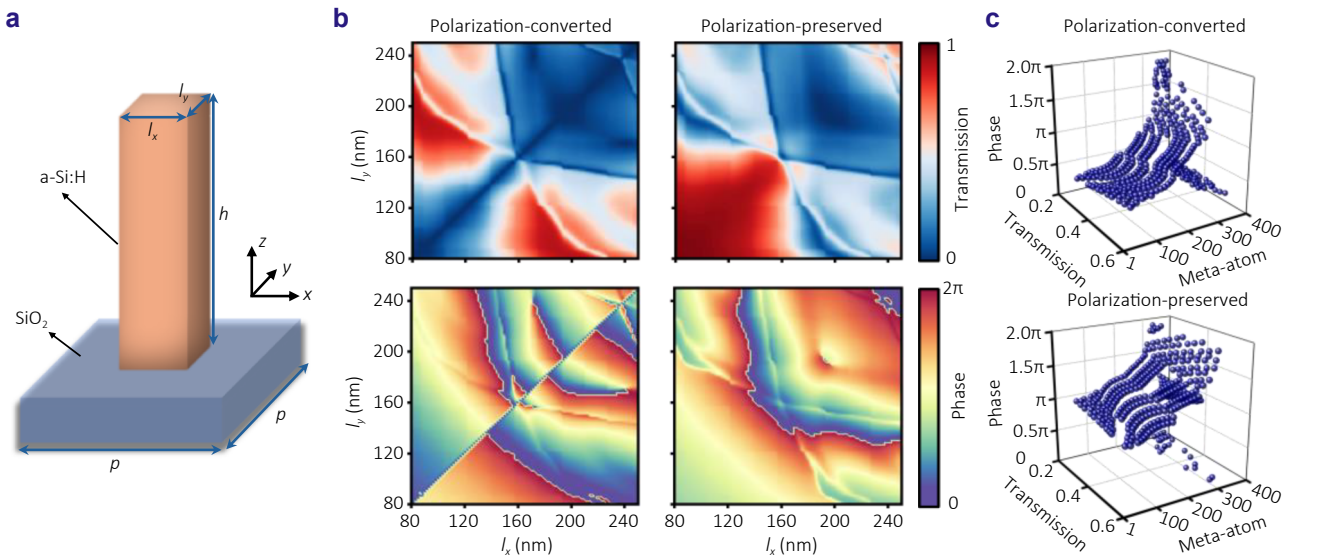


Fig. 2 | Meta-atom design and simulated optical responses. (a) Schematic of the anisotropic meta-atom composed of a-Si:H nanopillars on a SiO_2 substrate. (b) Simulated transmission and phase responses of the polarization-converted and polarization-preserved components as functions of the meta-atom geometric parameters. (c) Three-dimensional scatter plots summarizing the phase and transmission responses of the selected meta-atoms for the polarization-converted and polarization-preserved components. The meta-atom index serves as an identifier to correlate the phase and transmission responses of the same structure in both channels.

2.3 Metalens characterization

As proof of concept, the trichannel metalens based on aforementioned design principle is fabricated by electron beam lithography technology (see Supplementary Seciton 5). The scanning electron microscopy (SEM) images of the fabricated metalens can be seen in Fig. 3(a). All the samples used in experiments are fabricated with a-Si:H placed on a SiO_2 substrate with a diameter of 500 μm and a focal length of 430 μm at a target wavelength of 635 nm. Furthermore, to achieve clear spatial separation of the images from the three channels, we set the gradient deflection angle of the PB phase to 4° along the *x*-direction, thus imparting +4° and −4° deflection angles to Channels 1 and 3, respectively.

Figure 3(b) presents the experimentally measured PSFs of each channel at normal incidence (see Supplementary Section 6). To clearly observe the angular displacement of PSF, the horizontal axis in the plots was converted to angular coordinates. The metalens demonstrates clear focal spots and doughnut shapes in different channels, respectively, and its focal length of 430 μm has a good agreement with the designed parameters. Specifically, in Channel 2 (RCP-RCP and LCP-LCP), the output beam is tightly focused at 0° deflection angle, exhibiting a donut-shaped intensity profile characteristic of a first-order vortex beam. Based on the Jones matrix expression in Eq. (3), these two polarization-preserved channels are ideally expected to be equivalent because they experience the same spin-independent phase modulation (see Supplementary Section 7). Channel 1 (RCP-LCP) and Channel 3 (LCP-RCP) are separated at +4° and −4°, respectively, and Channel 1 produces a clear Gaussian focal spot, representing deflected focusing. At the same time, Channel 3 exhibits a larger doughnut-shaped PSF corresponding to a deflected focusing second-order vortex beam.

Next, we experimentally evaluate the wide-FOV capability and multi-channel parallel performance of the proposed metalens. In order to excite these three channels simultaneously, we fix both the input and output polarizations to *x*-linear polarization (XLP, defined as LP light with its electric field along the *x*-axis), thereby allowing simultaneous reception of all three channels. Subsequently, by rotating the rotation stage, different incident angles along the *x*-direction were introduced (see Supplementary Section 6). As shown in Fig. 3(c), the spatial positions and intensity profiles of the focal spots corresponding to each channel were measured in the same focal plane across an incident angle range from −10° to +10°. The results indicate that, with increasing incident angle, the focal spots of all three channels shift

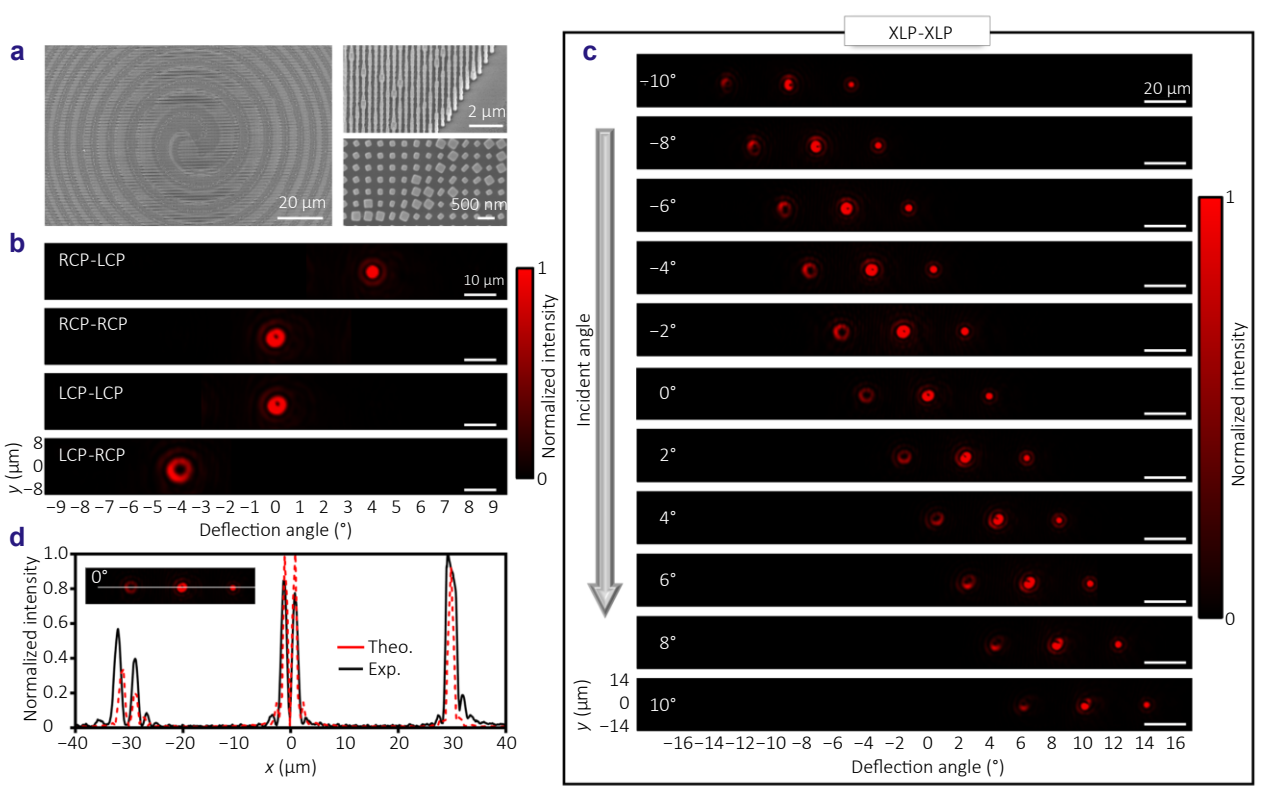


Fig. 3 | Experimental characterization of the trichannel metalens. (a) SEM images of the fabricated metalens. (b) Measured and normalized PSFs of the metalens in the different channels. (c) Experimentally measured PSFs at different incident angles. (d) Theoretical (Theo.) and experimental (Exp.) normalized intensity cross-sections along $y = 0$ at normal incidence. The inset figure shows the experimental results.

synchronously along the x-direction, accompanied by gradual changes in their intensity profiles. Notably, the doughnut-shaped focal spots corresponding to Channels 2 and 3 show pronounced asymmetry in their ring-shaped intensity distributions under oblique incidence. Specifically, the lateral displacement and shape variation of PSF along the x-direction are mainly caused by changes in the incident angle, while the deformation along the y-direction is mainly attributed to slight decentering between the laser beam and the metalens center, as well as minor axial misalignment in the optical system. These factors result in deviations of the actual incident wavefront relative to the designed condition, leading to localized non-ideal variations in the focal spot morphology. Furthermore, the intensity cross-sections along $y = 0$ in the focal plane at normal incidence are shown in Fig. 3(d). The full width at half maximum (FWHM) of focusing PSF is 1.36 μm for RCP-LCP in Channel 1, and the peak-to-peak (PTP) distances of the donut-shaped PSFs are 1.67 μm for RCP-RCP and 1.67 μm for LCP-LCP in Channel 2, and 3.75 μm for LCP-RCP in Channel 3, respectively. These experimental results are in excellent agreement with theoretical predictions (see Supplementary Section 8). Notably, the PTP distance ratio between Channels 2 and 3 is approximately 1:2, confirming that their associated OAM modes differ by a factor of two in their topological charges[51]. The measured efficiency, defined as the ratio of the power of the incident CP light to that in the transmitted polarization converted or preserved states, are 41.7% for RCP-LCP in Channel 1, 25.1% for RCP-RCP and 28.3% for LCP-LCP in Channel 2, and 14.5% for LCP-RCP in Channel 3, respectively.

2.4 Imaging results

The wide-FOV performance and multi-functional parallel imaging capability of the proposed metalens are experimentally verified using the USAF 1951 resolution test target. Figure 4(a) shows the optical images of Groups 6 and 7 of the USAF 1951 resolution test chart. The red-marked region, corresponding to Group 6 element 1 with a line width of 7.81 μm (64 lp/mm), is selected as the imaging target. The imaging performance of different channels is first evaluated under normal incidence, and the corresponding results are presented in Fig. 4(b) (see Supplementary Section 6). In these measurements, the output polarization is fixed to XLP to enable the simultaneous reception of imaging results from two channels, while the excited channels can be switched by varying the incident circular polarization. The line profiles shown on the right correspond to the imaging results of Channels 1, 2, and 3, respectively, thereby highlighting the bright-field imaging and multi-order edge enhanced imaging functionalities of the metalens. (The quantitative resolution characterization is provided in Supplementary Section 9.)

Under normal incidence, Channel 1 produces a conventional bright-field image characterized by a clear central bright region, sharp edges, and high contrast. Channel 2 exhibits a first-order differential-like response, where alternating bright and dark bands emphasize the object boundaries. Channel 3 shows second-order edge enhancement with a higher spatial modulation frequency, making it suitable for extracting finer structural details. Quantitatively, for the three-bar structure of the USAF target, the first-order edge detection channel yields six distinct intensity peaks corresponding to the six object edges, whereas the second-order channel exhibits an increased number of peaks with spatial positions that are interleaved with those of the first-order response. This difference in peak number and spatial distribution provides a clear criterion to distinguish the two differentiation orders, even though their normalized intensity profiles may appear similar in overall shape[52].

To further evaluate the wide-FOV performance, off-axis imaging experiments are subsequently carried out. In this configuration, both the input and output polarizations are fixed to XLP so that all three channels can be simultaneously excited and detected. By rotating the turntable to vary the incident angle, multi-channel parallel imaging results at different angles are obtained, as shown in Fig. 4(c). A theoretical validation of the angle-dependent response is provided in Supplementary section 8. Consistent with the theoretical predictions, all three imaging channels remain clearly distinguishable within −10° to +10° and shift synchronously across the imaging plane, demonstrating stable parallel multi-functional imaging over a wide-FOV. These observations demonstrate that the designed metalens can maintain stable, parallel, and multi-functional imaging over a wide-FOV.

As the incident angle increases, image blurring and distortion become more noticeable in the edge-enhanced channels. This behavior results from a combination of intrinsic angle dependent response and practical experimental factors. Especially, the second-order edge detection channel corresponds to a higher-order spatial differentiation operator, which produces a more structured PSF and is intrinsically more sensitive to wavefront perturbations and PSF deformation under oblique illumination[30,32,52]. Moreover, residual off-axis aberrations, angle dependent phase deviations, and unavoidable experimental imperfections such as minor optical misalignment, beam decentering, and fabrication tolerances can lead to more visible contrast nonuniformity and blur in the second-order response at larger incident angles. Particularly, small beam walk-off and pupil decentering during turntable scanning are difficult to eliminate, and such off-axis illumination errors more strongly impact the second-order differentiation response. Further improvement may be pursued by optimizing the meta-atom library toward a more robust angular phase response and higher polarization conversion efficiency.

To further assess the wide-FOV imaging performance of each channel, quarter-wave plates (QWPs) are introduced in

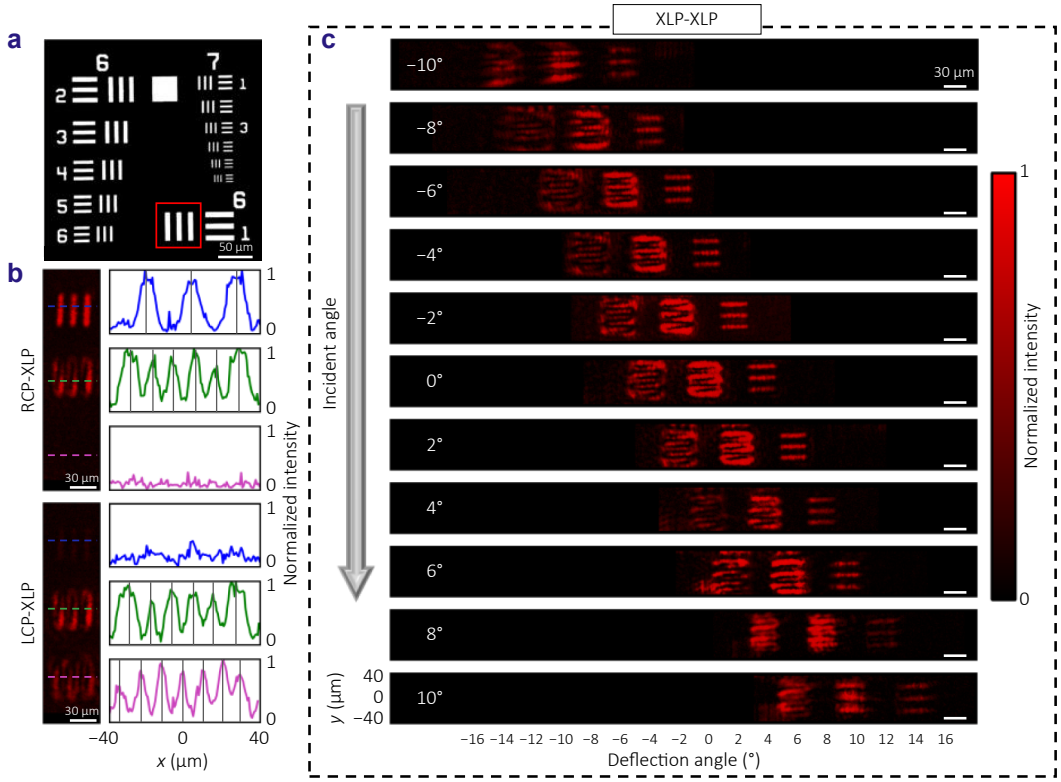


Fig. 4 | Resolution testing of the trichannel metalens. (a) The standard 1951 USAF resolution test chart as the input object. (b) Imaging results of the test target 6–1 marked by the red box in (a) in different channels. Right panel: the normalized intensity distribution along the corresponding dashed line. (c) Imaging results of the test target 6–1 marked by the red box in (a) at different incident angles under XLP-XLP configuration.

both the illumination and detection paths to isolate specific polarization combinations for independent characterization. Here, the USAF 1951 resolution target (Group 6) is selected as the imaging object. To obtain the distance between metalens and target, we first calibrate the effective magnification of the detection optics (objective lens + tube lens) using the resolution target (~23×) and then image the same target with the metalens to determine the overall system magnification (~46×). Consequently, we obtain the effective magnification contributed by the metalens during imaging (~2×) and the working distance (~645 μm). The corresponding imaging region is marked by solid white circles in Fig. 5(a), representing a 20° field angle, which corresponds to a radius of approximately 113 μm on the target. The one-dimensional intensity profiles along the lateral (green dashed lines) and vertical (blue dashed lines) directions in Fig. 5(a) are plotted in Fig. 5(b), where clear distinctions are observed across different channels. Thanks to the quadratic focusing phase profile, the metalens maintains stable imaging performance across all channels, with image contours remaining clear even toward the edges of the effective FOV.

It is worth emphasizing that this configuration enables a rapid, single-shot evaluation of the metalens wide-FOV capability, offering experimental simplicity and convenience. However, crosstalk between different channels and partial overlap of target regions may occur because the applied phase gradients introduce relatively small deflection angles. Increasing the deflection angle can enlarge the spatial separation between channels, although this typically reduces the effective FOV. Alternatively, implementing an off-axis focusing phase design can further increase spatial separation without sacrificing the FOV, but it usually requires a larger-area metalens, which increases the fabrication complexity and cost. In addition to channel overlapping, a certain degree of geometric distortion can occur at large field angles because the quadratic focusing phase maps the incident angle to a lateral focal displacement following a sine type relation, which deviates from the approximately linear paraxial mapping and may manifest as barrel like distortion or nonuniform magnification toward the edge of the effective FOV[53–55]. Since this contribution is largely deterministic, it can be compensated through post processing based on calibrated angle dependent image remapping, or more generally through hybrid optical computational imaging strategies. From an optical design perspective, the edge-of-FOV image quality could be improved by adopting more sophisticated aberration-compensated or ray-optimized phase architectures (e.g., phase profiles enabled by streamlined or catenary geometries), as well as multilayer, doublet, or cascaded metasurface designs that provide additional

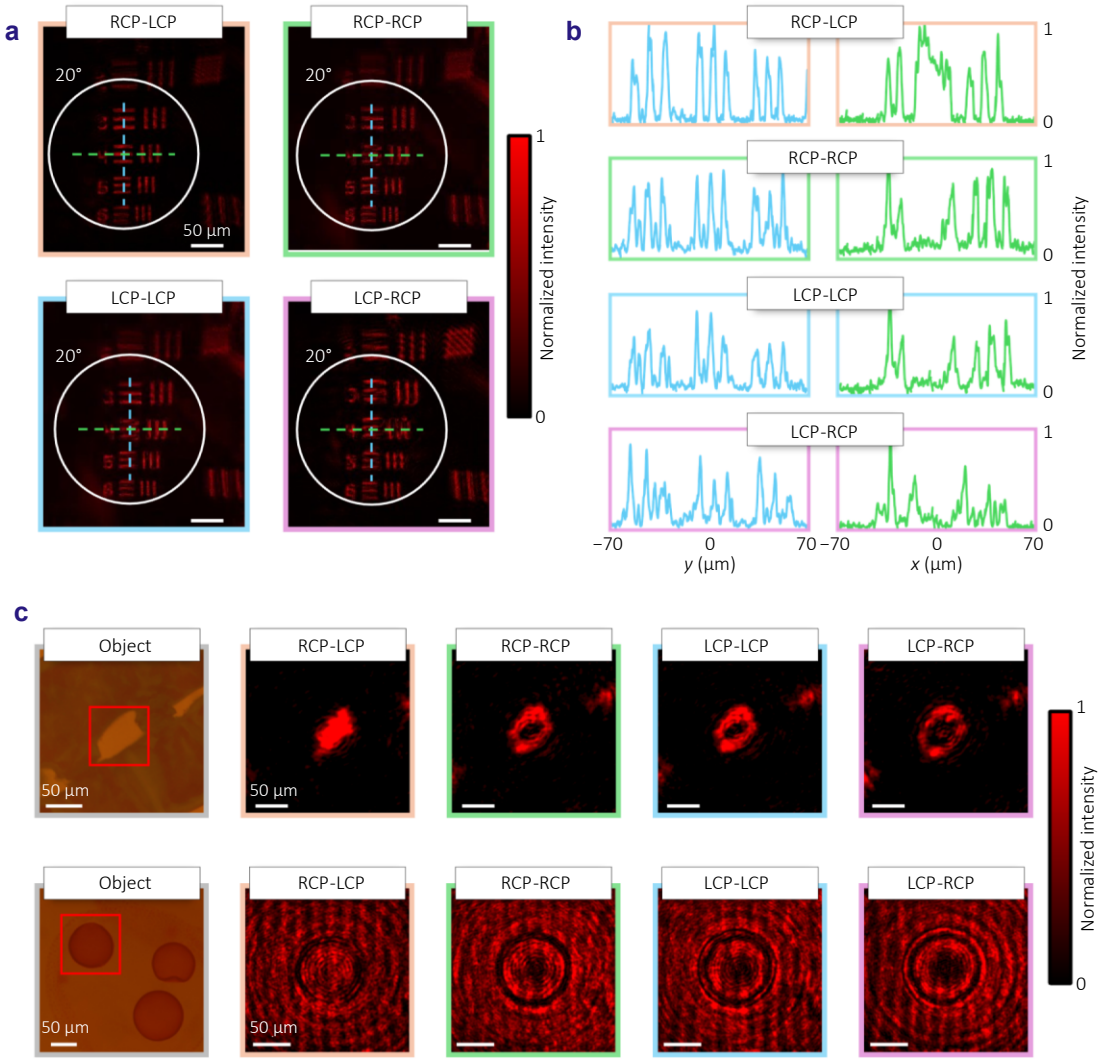


Fig. 5 | Wide-FOV imaging and bioimaging results of the trichannel metalens. (a) Imaging results of Group 6 of the test target in different channels at normal incidence. The FOV zones marked by solid circles are 20°. The distance between the metalens and the object is 645 μm. (b) The normalized intensity distribution along the corresponding dashed line in (a). (c) Bioimaging results of (top) Spirogyra conjugation and (bottom) Volvox cells. Left panel: optical microscope images. Right panel: imaging results of the portion marked by the red box in the left panel using the polarization-encoded trichannel metalens.

degrees of freedom for suppressing off-axis aberrations across a broader angular range, while typically requiring increased design and fabrication complexity[49,56–60]. These approaches represent promising future directions to extend the usable FOV and improve edge-of-field fidelity while maintaining compact meta-optical integration.

Having established the wide-FOV behavior using the resolution target in Fig. 5(a) and 5(b) (where edge-of-field distortion can be directly visualized), we next demonstrate the practical bioimaging utility of the trichannel metalens in Fig. 5(c). Due to the biological specimens being imaged within the selected region of interest, the edge-of-FOV distortion discussed above is not a dominant visual factor in these demonstrations. We employ the trichannel metalens to image two representative biological specimens (Spirogyra conjugation and Volvox) under both bright-field and multi-order edge-enhanced imaging channels. Spirogyra is a filamentous green alga with a chain-like cellular arrangement and distinct cell walls, often used in studies of cell division and conjugation. Volvox is a spherical multicellular alga composed of hundreds to thousands of cells forming a hollow spherical structure, making it an excellent model for exploring cellular differentiation and multicellular coordination.

Under Channel 1 (bright-field imaging), due to the high transparency of both the intercellular gaps in Spirogyra and the spherical structure of Volvox, the cell boundaries are poorly defined, and the image contrast is relatively low, making it difficult to clearly distinguish structural details. In contrast, in Channel 2 and Channel 3 (corresponding to

first-order and second-order edge-enhanced imaging), the cell outlines are significantly enhanced, and finer structural details become more visible. For instance, in the Spirogyra images, we can observe intercellular connections and membrane structures; while in Volvox, its spherical configuration and cell distribution boundaries are rendered with high contrast, with a characteristic donut-shaped shadow appearing at the center. Notably, in the higher-order edge-enhanced images, the central dark region becomes larger, indicating that more low-frequency information is suppressed, thereby making the cell edges sharper and more distinct. These experimental results demonstrate that the proposed trichannel metalens is capable of effectively enhancing the structural edges of biological samples while achieving bright imaging, offering great potential for applications in real-time cellular response monitoring, cell morphology analysis, and organoid-based drug screening.

3 Conclusion

In this work, we have proposed and experimentally demonstrated a polarization-encoded trichannel metalens that enables simultaneous bright-field imaging and multi-order edge detection within a single, compact, and static optical platform. By encoding distinct combinations of incident and transmitted circular polarizations and introducing spin-dependent gradient phase profiles, the metalens spatially separates three imaging modalities, bright-field, first-order edge detection, and second-order edge detection, without requiring dynamic modulation or additional optical components. Since the PG phase is shared by all channels, while only the polarization-converted components acquire an additional spin-dependent PB phase, these three channels are intrinsically coupled and cannot be independently programmed in a fully arbitrary manner.

The designed metalens achieves multi-functional, parallel imaging across a wide-FOV (20°), with experimentally validated focusing efficiencies of 41.7% (RCP-LCP in Channel 1), 25.1% (RCP-RCP in Channel 2), 28.3% (LCP-LCP in Channel 2), and 14.5% (LCP-RCP in Channel 3). In general, the achievable FOV of a metalens is jointly influenced by its NA and the extent to which off-axis phase errors and aberrations can be tolerated or compensated in the design. In our single-layer platform, the selected NA primarily determines the resolution and light-collection capability, while the demonstrated wide-FOV operation is mainly enabled by the adopted quadratic focusing phase that provides a deterministic angular-to-spatial mapping under oblique incidence. These efficiency values reflect the intentional redistribution of optical power among multiple polarization-encoded channels to support simultaneous acquisition of complementary imaging modalities, rather than optimization toward a single high-throughput imaging function. Compared with conventional refractive lenses or single-function metalenses that prioritize maximum efficiency in a single imaging channel, the proposed design offers distinct advantages for advanced biomedical imaging scenarios, where parallel access to bright-field and edge-enhanced information is often more critical than maximizing intensity throughput alone. In particular, the ability to simultaneously extract intensity and spatial differentiation information facilitates the visualization of weakly scattering and transparent samples, reducing reliance on additional staining, contrast agents, or sequential imaging steps. This capability is further validated through biological imaging experiments using Spirogyra conjugation and Volvox specimens, where the edge-enhanced imaging channels effectively highlight fine cellular boundaries and spatial textures that are difficult to observe in conventional bright-field images, underscoring the potential of the proposed platform for real-time, label-free biological imaging.

Beyond polarization multiplexing based on Jones matrix engineering, recent studies have also demonstrated complementary strategies for parallel multi-functional imaging. For example, off-axis phase engineering can spatially separate different imaging functionalities by superimposing multiple off-axis phase functions, enabling synchronous acquisition of bright-field and spiral phase contrast images within a single metasurface[47]. In addition, staggered or superpixel-based meta-atom arrangements provide an alternative route to complex amplitude control, which can be leveraged to realize broadband multi-order spatial differentiation and further combined with channel-dependent deflection phases for parallel readout[32]. These approaches suggest feasible future directions to extend the channel number, enrich the accessible imaging operators, and further optimize power allocation and channel separation within compact meta-optical platforms.

In summary, the demonstrated polarization-encoded trichannel metalens provides a system-levelly simple and wide-FOV route to parallel multi-modal imaging with straightforward channel addressing (via polarization). It offers a scalable, multi-functional, and compact imaging solution with promising applications in biomedical imaging, edge-aware machine vision, and optical computing.

References

1. Ersoy OK. *Diffraction, Fourier Optics and Imaging* (Wiley, Hoboken, 2007).
2. Ishimaru A. *Electromagnetic Wave Propagation, Radiation, and Scattering: From Fundamentals to Applications* 2nd ed (Wiley, Hoboken, 2017).
3. Chen HT, Taylor AJ, Yu NF. A review of metasurfaces: physics and applications. *Rep Prog Phys* **79**, 076401 (2016).
4. Hsiao HH, Chu CH, Tsai DP. Fundamentals and applications of metasurfaces. *Small Methods* **1**, 1600064 (2017).
5. Huang LL, Zhang S, Zentgraf T. Metasurface holography: from fundamentals to applications. *Nanophotonics* **7**, 1169–1190 (2018).
6. Jiang Q, Jin GF, Cao LC. When metasurface meets hologram: principle and advances. *Adv Opt Photonics* **11**, 518–576 (2019).
7. Chen SQ, Liu WW, Li ZC et al. Metasurface-empowered optical

multiplexing and multifunction. *Adv Mater* **32**, 1805912 (2020).
8. Jung C, Kim G, Jeong M et al. Metasurface-driven optically variable devices. *Chem Rev* **121**, 13013–13050 (2021).
9. Qiu CW, Zhang T, Hu GW et al. Quo vadis, metasurfaces. *Nano Lett* **21**, 5461–5474 (2021).
10. Yang H, Ou K, Wan HY et al. Metasurface-empowered optical cryptography. *Mater Today* **67**, 424–445 (2023).
11. Kim Y, Li XT, Tang P et al. Spin-dependent phenomena of metaoptics. *ACS Photonics* **12**, 16–33 (2025).
12. Li XT, Lee HT, Han D et al. Metasurface-driven sensing in terahertz region: principles, applications, fabrication, and challenges. *Adv Mater Technol* **10**, e00886 (2025).
13. Jia TX, Jeon Y, Feng L et al. Superchirality induced ultrasensitive chiral detection in high-*Q* optical cavities. *Opto-Electron Adv* **8**, 250079 (2025).
14. Yu NF, Genevet P, Kats MA et al. Light propagation with phase discontinuities: generalized laws of reflection and refraction. *Science* **334**, 333–337 (2011).
15. Sun SL, He Q, Xiao SY et al. Gradient-index meta-surfaces as a bridge linking propagating waves and surface waves. *Nat Mater* **11**, 426–431 (2012).
16. Arbabi A, Arbabi E, Horie Y et al. Planar metasurface retroreflector. *Nat Photonics* **11**, 415–420 (2017).
17. Li M, Shen L, Jing LQ et al. Origami metawall: mechanically controlled absorption and deflection of light. *Adv Sci* **6**, 1901434 (2019).
18. Juliano Martins R, Marinov E, Ben Youssef MA et al. Metasurface-enhanced light detection and ranging technology. *Nat Commun* **13**, 5724 (2022).
19. Yin XB, Ye ZL, Rho J et al. Photonic spin Hall effect at metasurfaces. *Science* **339**, 1405–1407 (2013).
20. Zhou JX, Qian HL, Hu GW et al. Broadband photonic spin Hall meta-lens. *ACS Nano* **12**, 82–88 (2018).
21. Ling XH, Guan FX, Cai XD et al. Topology-induced phase transitions in spin-orbit photonics. *Laser Photonics Rev* **15**, 2000492 (2021).
22. Kim M, Lee D, Yang Y et al. Reaching the highest efficiency of spin Hall effect of light in the near-infrared using all-dielectric metasurfaces. *Nat Commun* **13**, 2036 (2022).
23. Ke YG, Bian YF, Tang Q et al. Rotational photonic spin Hall effect. *Nanophotonics* **12**, 4361–4373 (2023).
24. Tang P, Li XT, Kim Y et al. Spin Hall effect of light in a dichroic polarizer for multifunctional edge detection. *ACS Photonics* **11**, 4170–4176 (2024).
25. Kim Y, Tang P, Jung C et al. Topological vortex transition induced by spin hall effect of light for tunable humidity sensing and imaging. *Laser Photonics Rev* **19**, e00581 (2025).
26. Chen WT, Zhu AY, Sanjeev V et al. A broadband achromatic metalens for focusing and imaging in the visible. *Nat Nanotechnol* **13**, 220–226 (2018).
27. Paniagua-Domínguez R, Yu YF, Khaidarov E et al. A metalens with a near-unity numerical aperture. *Nano Lett* **18**, 2124–2132 (2018).
28. Wang SM, Wu PC, Su VC et al. A broadband achromatic metalens in the visible. *Nat Nanotechnol* **13**, 227–232 (2018).
29. Balli F, Sultan M, Lami SK et al. A hybrid achromatic metalens. *Nat Commun* **11**, 3892 (2020).
30. Badloe T, Seong J, Rho J. Trichannel spin-selective metalenses. *Nano Lett* **23**, 6958–6965 (2023).
31. Wang RX, Ansari MA, Ahmed H et al. Compact multi-foci metalens spectrometer. *Light Sci Appl* **12**, 103 (2023).
32. Huo PC, Tan L, Jin YQ et al. Broadband and parallel multiple-order optical spatial differentiation enabled by Bessel vortex modulated metalens. *Nat Commun* **15**, 9045 (2024).
33. Tang P, Jeon Y, Li XT et al. Switchable bright-field imaging and corner detection with an electrically tunable metalens. *Adv Opt Mater* **13**, 2500981 (2025).
34. Kim Y, Lee J, Yeo WH et al. Rapid polarization-controlled depth sensing and imaging with an electrically tunable metalens. *Nano Lett* **25**, 9394–9401 (2025).
35. Huang LL, Chen XZ, Mühlenbernd H et al. Three-dimensional optical holography using a plasmonic metasurface. *Nat Commun* **4**, 2808 (2013).
36. Zheng GX, Mühlenbernd H, Kenney M et al. Metasurface holograms reaching 80% efficiency. *Nat Nanotechnol* **10**, 308–312 (2015).
37. Kang H, Kim H, Kim K et al. Printable spin-multiplexed metasurfaces for ultraviolet holographic displays. *ACS Nano* **18**, 21504–21511 (2024).
38. Yin YY, Jiang Q, Wang HB et al. Multi-dimensional multiplexed metasurface holography by inverse design. *Adv Mater* **36**, 2312303 (2024).
39. Choi M, Kim J, Moon S et al. Roll-to-plate printable RGB achromatic metalens for wide-field-of-view holographic near-eye displays. *Nat Mater* **24**, 535–543 (2025).
40. Park C, Jeon Y, Rho J. 36-channel spin and wavelength co-multiplexed metasurface holography by phase-gradient inverse design. *Adv Sci* **12**, 2504634 (2025).
41. Cai XD, Tang R, Zhou HY et al. Dynamically controlling terahertz wavefronts with cascaded metasurfaces. *Adv Photonics* **3**, 036003 (2021).
42. Du K, Barkaoui H, Zhang XD et al. Optical metasurfaces towards multifunctionality and tunability. *Nanophotonics* **11**, 1761–1781 (2022).
43. Ko B, Badloe T, Yang Y et al. Tunable metasurfaces via the humidity responsive swelling of single-step imprinted polyvinyl alcohol nanostructures. *Nat Commun* **13**, 6256 (2022).
44. Li QS, Cai XD, Liu T et al. Gate-tuned graphene meta-devices for dynamically controlling terahertz wavefronts. *Nanophotonics* **11**, 2085–2096 (2022).
45. Ni YB, Chen C, Wen S et al. Computational spectropolarimetry with a tunable liquid crystal metasurface. *eLight* **2**, 23 (2022).
46. Badloe T, Kim Y, Kim J et al. Bright-field and edge-enhanced imaging using an electrically tunable dual-mode metalens. *ACS Nano* **17**, 14678–14685 (2023).
47. Zhang YZ, Lin PC, Huo PC et al. Dielectric metasurface for synchronously spiral phase contrast and bright-field imaging. *Nano Lett* **23**, 2991–2997 (2023).
48. Jung C, Lee E, Rho J. The rise of electrically tunable metasurfaces. *Sci Adv* **10**, eado8964 (2024).
49. Li XT, Cai XD, Liu C et al. Cascaded metasurfaces enabling adaptive aberration corrections for focus scanning. *Opto-Electron Adv* **7**, 240085 (2024).
50. Yang Y, Yoon G, Park S et al. Revealing structural disorder in hydrogenated amorphous silicon for a low-loss photonic platform at visible frequencies. *Adv Mater* **33**, 2005893 (2021).
51. Chen SM, Cai Y, Li GX et al. Geometric metasurface fork gratings for vortex-beam generation and manipulation. *Laser Photonics Rev* **10**, 322–326 (2016).
52. Qiu XD, Zhang JC, Fan YB et al. Metasurface enabled high-order differentiator. *Nat Commun* **16**, 2437 (2025).
53. Pu MB, Li X, Guo YH et al. Nanoapertures with ordered rotations: Symmetry transformation and wide-angle flat lensing. *Opt Express* **25**, 31471–31477 (2017).
54. Guo YH, Ma XL, Pu MB et al. High-efficiency and wide-angle beam steering based on catenary optical fields in ultrathin metalens. *Adv Opt Mater* **6**, 1800592 (2018).
55. Martins A, Li KZ, Li JT et al. On metalenses with arbitrarily wide field of view. *ACS Photonics* **7**, 2073–2079 (2020).
56. Yang F, Shalaginov MY, Lin HI et al. Wide field-of-view metalens: a tutorial. *Adv Photonics* **5**, 033001 (2023).
57. Zhang F, Pu MB, Li X et al. Extreme-angle silicon infrared optics enabled by streamlined surfaces. *Adv Mater* **33**, 2008157 (2021).

58. Go GH, Park CH, Woo KY et al. Scannable dual-focus metalens with hybrid phase. *Nano Lett* **23**, 3152–3158 (2023).
59. Javed Satti A, Lee E, Javed I et al. Nearly 180° field-of-view metalens for miniaturized imaging systems. *Laser Photonics Rev* **20**, e00098 (2026).
60. Shalaginov MY, An SS, Yang F et al. Single-element diffraction-limited fisheye metalens. *Nano Lett* **20**, 7429–7437 (2020).

Acknowledgements

This research was supported by the POSCO-POSTECH-RIST Convergence Research Center program funded by POSCO, and the National Research Foundation (NRF) grant (RS-2024-00462912) funded by the Ministry of Science and ICT (MSIT) of the Korean government. T.B acknowledges the Regional Innovation System & Education (RISE) program through the Sejong RISE Center, funded by the Ministry of Education (MOE) and the Sejong City, Republic of Korea (2025-RISE-08-001). Y.K acknowledges the Presidential Science fellowship funded by the MSIT of the Korean government. Y.J. acknowledges the NRF Ph.D. fellowship (RS-2025-25437554) funded by the Ministry of Education (MOE) of the Korean government. H.K. acknowledges the POSCO Asia fellowship and Yuhan Foundation *New Ilhan* fellowship. Y.-S.R. acknowledges a grant of Korean ARPA-H Project through the Korea Health Industry Development Institute (KHIDI), funded by the Ministryof Health & Welfare, Republic of Korea (Grant number: RS-2025-25454431). X.L. acknowledges the China Scholarship Council (202306890039). L.D. acknowledges the China Scholarship Council (202506030039).

Author contributions

J.R. and T.B. conceived the idea and initiated the project. X.L. conducted the numerical simulations, performed the experiments, and prepared the original draft. Y.K. helped with the experiments and manuscript preparation. Y.J. fabricated the samples and manuscript preparation. J.S. assisted with sample fabrication. J.K. assisted the preparation of the biological cells. P.T., S.Q., H.K., B.Y., D.J., W.L., X.C., L.D., Y.-S.R., and J.S. assisted in data and results analysis. All authors confirmed the final manuscript. J.R. guided the entire work.

Competing interests

The authors declare no competing interests.

Data availability

The data that supports the findings of this study is available from the corresponding author upon reasonable request.

Open Access This article is licensed under a Creative Commons Attribution 4.0 International License, which permits use, sharing, adaptation, distribution and reproduction in any medium or format, as long as you give appropriate credit to the original author(s) and the source, provide a link to the Creative Commons license, and indicate if changes were made. To view a copy of this license, visit http://creativecommons.org/licenses/by/4.0/
©The Author(s) 2026.
Published by Editorial Office of *Opto-Electronic Advance*, Institute of Optics and Electronics, Chinese Academy of Sciences.

Opto-Electronic Journals Group
www.oejournal.org
Scan for Article PDF